

## Article

# Methanogenesis Potentials: Insights from Mineralogical Diagenesis, SEM and FTIR Features of the Permian Mikambeni Shale of the Tuli Basin, Limpopo Province of South Africa

George Oluwole Akintola <sup>1,\*</sup>, Francis Amponsah-Dacosta <sup>1</sup>, Steven Rupprecht <sup>2</sup>, Nithyadharseni Palaniyandy <sup>3</sup>, Sphiwe Emmanuel Mhlongo <sup>1</sup>, Wilson Mugeru Gitari <sup>4</sup> and Joshua Nosa Edokpayi <sup>5</sup>

- <sup>1</sup> Department of Mining and Environmental Geology, University of Venda, Thohoyandou 0950, South Africa; francis.dacosta@univen.ac.za (F.A.-D.); emmanuel.mhlongo@univen.ac.za (S.E.M.)
- <sup>2</sup> Department of Mining Engineering, University of Johannesburg, Johannesburg 2006, South Africa; stevenr@uj.ac.za
- <sup>3</sup> Energy Centre, Council for Scientific and Industrial Research (CSIR), Pretoria 0184, South Africa; npalaniyandy@csir.co.za
- <sup>4</sup> Department of Ecology Resource Management, University of Venda, Thohoyandou 0950, South Africa; mugera.gitari@univen.ac.za
- <sup>5</sup> Department of Hydrology and Water Resources, University of Venda, Thohoyandou 0950, South Africa; joshua.edokpayi@univen.ac.za
- \* Correspondence: georgeakintola540@gmail.com



**Citation:** Akintola, G.O.; Amponsah-Dacosta, F.; Rupprecht, S.; Palaniyandy, N.; Mhlongo, S.E.;

Gitari, W.M.; Edokpayi, J.N.

Methanogenesis Potentials: Insights from Mineralogical Diagenesis, SEM and FTIR Features of the Permian Mikambeni Shale of the Tuli Basin, Limpopo Province of South Africa. *Minerals* **2021**, *11*, 651. <https://doi.org/10.3390/min11060651>

Academic Editor:

Leszek Marynowski

Received: 20 May 2021

Accepted: 2 June 2021

Published: 19 June 2021

**Publisher's Note:** MDPI stays neutral with regard to jurisdictional claims in published maps and institutional affiliations.



**Copyright:** © 2021 by the authors. Licensee MDPI, Basel, Switzerland. This article is an open access article distributed under the terms and conditions of the Creative Commons Attribution (CC BY) license (<https://creativecommons.org/licenses/by/4.0/>).

**Abstract:** Carbonaceous shale is more topical than ever before due to the associated unconventional resources of methane. The use of FTIR, SEM-EDX, and mineralogical analyses has demonstrated a promising approach to assess methanogenesis potentials in a more rapid and reliable manner for preliminary prospecting. Representative core samples from the borehole that penetrated the carbonaceous Mikambeni shale Formations were investigated for methanogenesis potentials. The absorption band stretches from 1650 cm<sup>-1</sup> to 1220 cm<sup>-1</sup> in wavenumber, corresponding to C-O stretching and OH deformation of acetic and phenolic groups in all studied samples, thereby suggesting biogenic methanogenesis. The CO<sub>2</sub> was produced by decarboxylation of organic matter around 2000 cm<sup>-1</sup> and 2300 cm<sup>-1</sup> and served as a source of the carboxylic acid that dissolved the feldspar. This dissolution process tended to release K<sup>+</sup> ions, which facilitated the illitization of the smectite minerals. The SEM-EDX spectroscopy depicted a polyframboidal pyrite structure, which indicated a sulfate reduction of pyrite minerals resulting from microbial activities in an anoxic milieu and causes an increase in alkalinity medium that favors precipitation of dolomite in the presence of Ca and Mg as burial depth increases. The contact diagenesis from the proximity of Sagole geothermal spring via Tshipise fault is suggested to have enhanced the transformation of smectite to chlorite via a mixed layer corrensites in a solid-state gradual replacement reaction pathway. The presence of diagenetic chlorite mineral is characteristic of low-grade metamorphism or high diagenetic zone at a temperature around 200 °C to 230 °C and corresponds to thermal breakdown of kerogen to methane at strong absorption band around 2850 cm<sup>-1</sup> and 3000 cm<sup>-1</sup>, indicating thermal methanogenesis.

**Keywords:** methanogenesis potentials; biogenic methanogenesis; thermal methanogenesis; carbonaceous shale; carboxylic; illitization; chloritization; framboidal pyrite

## 1. Introduction

Carbonaceous shale has been more topical than ever before due to the associated unconventional resources for energy supply. Shale constitutes an essential component of unconventional gas generation due to the global clamor for an energy transition from heavy

greenhouse domination to low-carbon natural gases [1–3]. With respect to climate change moderation, carbonaceous shale has been identified to promote a short-term accelerated action to achieve the 2015 Paris agreement climate targets of keeping the global temperature increases below 2 °C. In recent studies [4,5], shale gas exploration has been prioritized in the US from 2006 to 2020, cutting off well over 430 million tonnes of CO<sub>2</sub> emission and accounting for over 30% of the financial fiscal year [6,7]. In contrast to conventional shale source rocks, carbonaceous shales tend to host natural gas under a low pressure and extremely low permeability but extractable using horizontal well-drilling and hydraulic fracturing technologies [8–11].

Despite many decades of research in carbonaceous shale, a reliable and rapid discriminative approach to identify a potential methane gas-bearing rock remains elusive. However, some studies have used petrographic and sedimentological properties [12,13], geophysical properties [14–16], and geochemical and mineralogical characteristics [17–20] to attribute most organic matter transformation to their burial. Furthermore, there is extensive recent literature [21–29] on the successful use of an organic geochemical method to determine petrophysical properties such as total organic carbon (TOC), thermal maturity, vitrinite content, and desorbed gas composition. Undoubtedly, these investigative approaches provide deterministic information rather than discrimination at the preliminary exploratory stage [30]. The discriminative approach identifies sweet-spot targets for further detailed and determinative investigations, which require huge cost implications.

This research provides information on methane formation during the transformation of organic components of organic-rich sedimentary deposits. It applies evidence from mineralogical, structural, and functional-group features of the carbonaceous Mikambeni shale in the Tuli Basin. The Permian Tuli Basin is known as the Limpopo-area Karoo Basin, hosting coal resources used to power a coal-fired plant for electricity generation in the northeastern region of South Africa [31–34]. The potential for methanogenesis sources has not been given proper attention in the burial depth, having a thickness of 1 km or less.

### Study Area

The Tuli Basin is a trans-frontier depozone that straddles the triple junction of South Africa, Zimbabwe, and Botswana situated within latitudes 29°36′22.19″ E and 28°25′23.15″ E and longitudes 23°11′24.45″ S and 22°43′24.54″ S (Figure 1). This basin is a back-bulge structural depression that resulted from crustal subsidence due to tectonic regimes adjacent to the Cape Fold Belt (CFB) orogenic belt. The subsidence controls the accommodation space that preserves the Carboniferous–Jurassic sedimentary sequence of the Tuli Basin in South Africa [35,36]. The succession of formations from oldest to youngest is the Tshidzi, Madzaringwe, Mikambeni, Fripp, Solitude, Klopperfontein, Bosbokpoort, and Clarens Formations [37] (Figure 1).

The Mikambeni Formation consists of the Permian black carbonaceous shale intercalated with coal seams and alternating sandstone and siltstone [31]. The thickness of the Mikambeni Formation ranges from 60 to 100 m, corresponding to the proximal and distal points. The variation in shale thickness is interpreted to be caused by basin tectonics and differential subsidence trends as transporting river flowed from the northwest to deposit more sediments towards the southeast direction of the basin [34]. The coal seam associated with the Tuli Basin is dominated by collotelinite, suggesting organic matter input from cellulose and woody tissues of the higher terrestrial plant. Based on lithofacies description, the shale color and content suggest a reducing condition associated with oxygen deficiency causing decay of fauna and flora or plant organisms. Given the overall sedimentary sequence, the deposition represents a fluvial-to-aeolian milieu. This deposition reflects different paleo-climatic overprints of different ages spanning from the Permian to the Jurassic Period [38]. Besides the lignin, the cellulose and tannins of vascular plants *dicroidium* are partly responsible for the main coal seam associated with the carbonaceous shale of the Mikambeni Formation [31,39]. In contrast to lithofacies of Mkambeni, the Tshidzi Formation shows non-sorted to poorly sorted argillaceous or sandy

sediments with particles size up to 2 m in diameter. This argillaceous diamictite suggests a glacial or fluvioglacial environment resulting from a low energy level of mudflow to deposit well-sorted sediments. There is a progressive change from reducing or anoxic to the oxidizing environment as shale formations become younger. The Triassic black shale at the lower unit of Solitude Formation has a dark grey shale and grey shale towards overlying Bosbokpoort and Clarens Formations [38]. This color variation reflects a progressive fall in water level where sediments are deposited on floodplains of meandering rivers under dry and oxidizing conditions. The preponderance of red calcareous concretions of overlying the Bosbokpoort further support an oxidizing environment towards the upper Tshipise Basin.

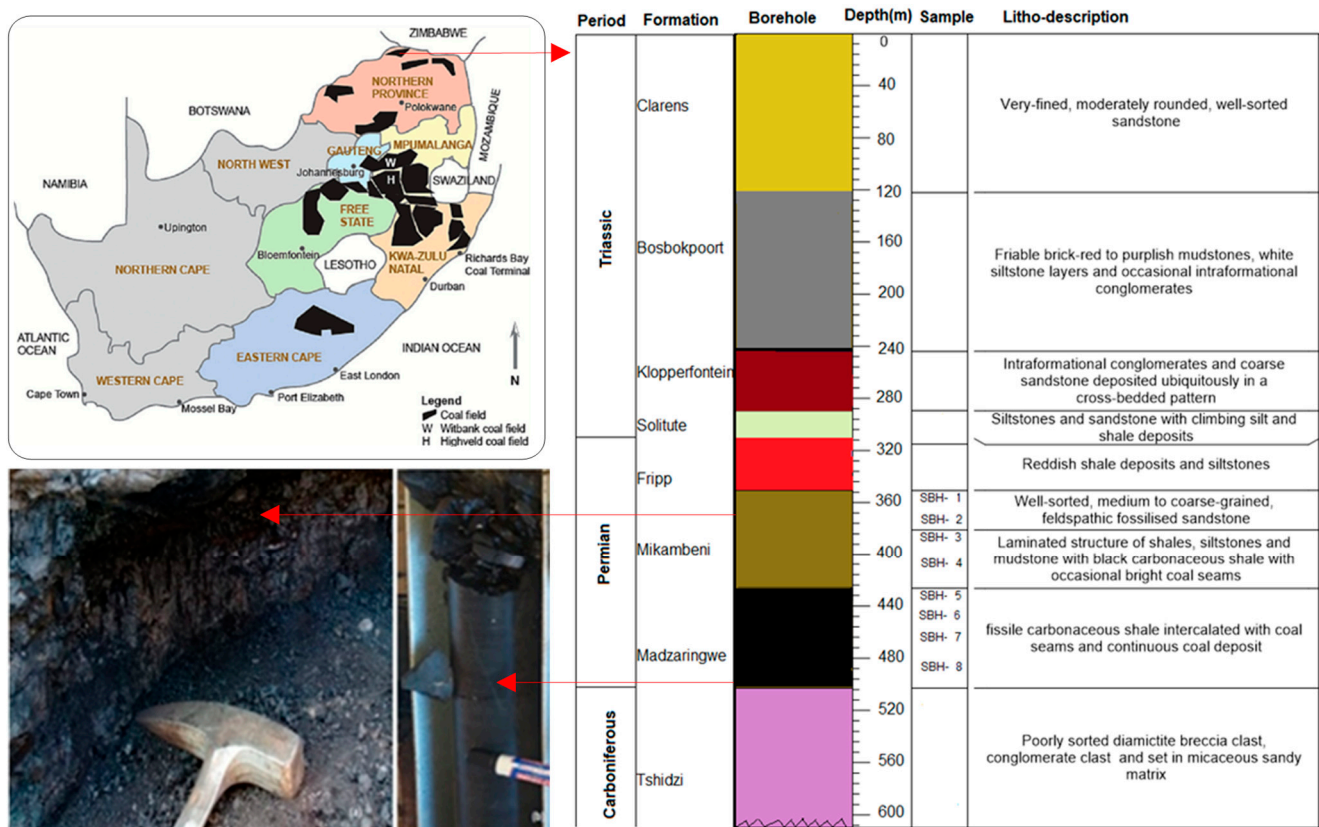


Figure 1. Map and sedimentary sequence of the Tuli Backbulge Basin.

## 2. Materials and Methods

Mineralogical identification of 16 core samples from the borehole that penetrated the carbonaceous Mikambeni shale Formations at different depths was determined using X-ray diffraction (XRD) at Council for Scientific and Industrial Research (CSIR) Pretoria (Figure 2).

Based on the lithological facies, 8 representative shale samples corresponding to the formations were selected and pulverized in an agate mortar. The clay fractions were dispersed in 0.7 mg/mL of distilled water and put in an ultrasonic water bath for 40 s to prevent the flocculation of particles [40]. Afterward, the air-dried samples were treated with ethylene glycolation to identify smectite minerals and dimethyl sulphoxide to differentiate kaolinite from chlorite [41]. Samples were tightly mounted on oriented sample holder with very little pressure using black loading preparation technique using PANalytical X'Pert Pro-powder diffractometer equipped with X'Celerator detector coupled with receiving slits, variable divergence, and Fe-filtered Cu-K $\alpha$  radiation at the Energy Centre CSIR Pretoria. While the receiving slit was positioned at 0.040°, the counting area was from 2 to 80° on a 2 $\theta$  scale at 1.5 s [42]. The interstratified I/S minerals were measured on a less than 2  $\mu$ m fraction of air-dried samples using Cu-K $\alpha$  radiation [43]. Semi-quantitative

mineral measurements were obtained using single line fitting of TOPAS software while the detection limits remained 1%.

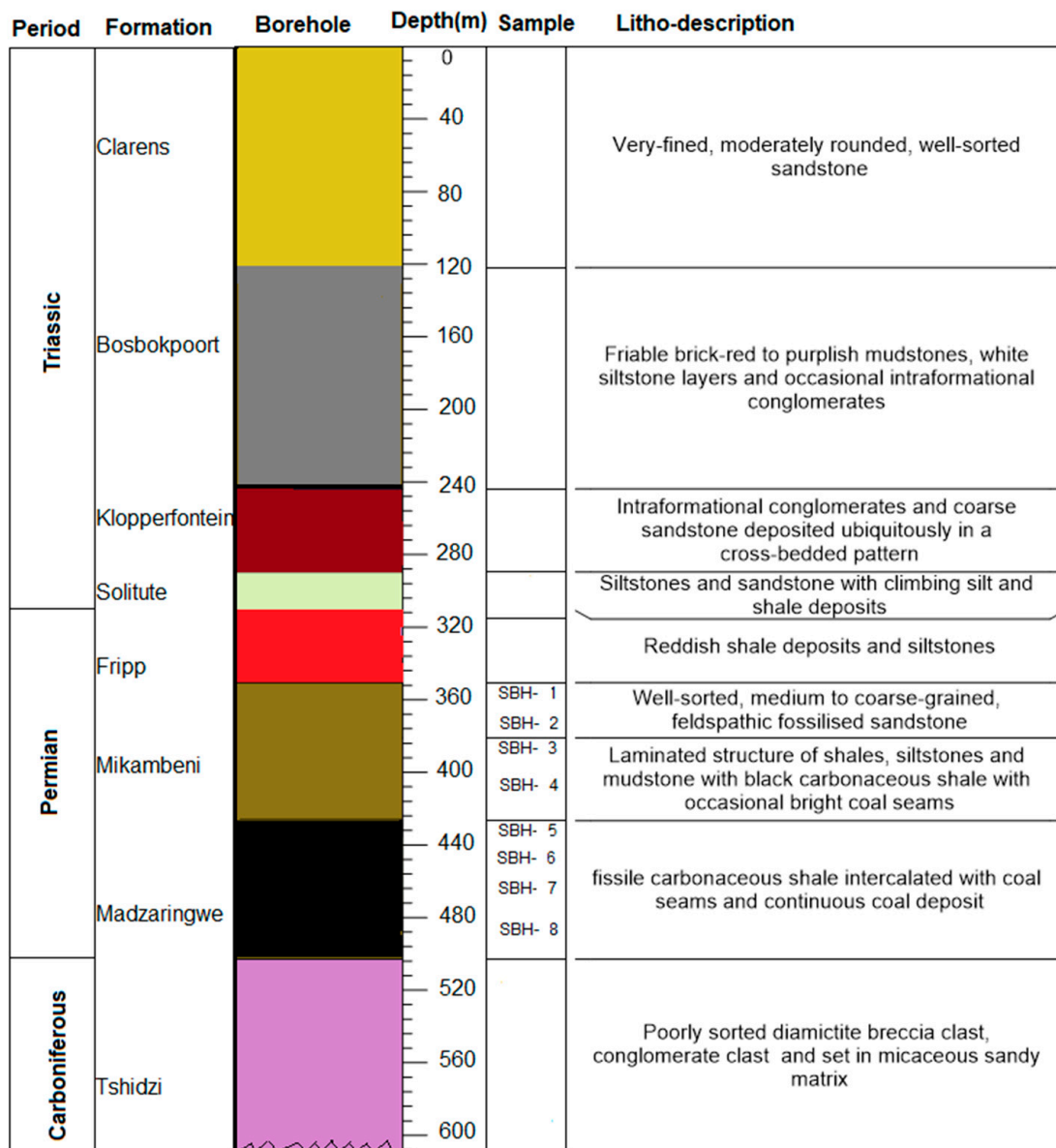


Figure 2. Stratigraphic column of the studied borehole showing lithologic description and carbonaceous shale sampling depth.

The functional group information was provided by the Fourier Transform Infrared (FTIR) Alpha Bruker spectrophotometer at the University of Venda, Limpopo. Pulverized samples were placed in the measurement position of the spectrometer and scanned between a minimum and maximum wavelength range of 500 and 4000 cm<sup>-1</sup>, respectively. The absorbance spectrum depicts the crystalline phases which reflect their functional group.

A Zeiss EVO MA15 scanning electron microscope (SEM) equipped with a tungsten filament and a Bruker energy-dispersive X-ray (EDX) spectrometer were used for the morphological analysis. The system was operated under a high system vacuum, approximately 7.03 e to 007 mbar. The electron beam was generated with an accelerating voltage of 20 kV and a probe current of approximately 2nA. The sample was sprinkled onto a carbon tape substrate and carbon-coated prior to being loaded into the SEM. A secondary electron detector was used to produce images at 300×, 600×, and 900× magnification. Some of these particles are out of focus, owing to the three-dimensional depth loss of informa-

tion; focusing one part results in the other being out of focus on some of these images, particularly at high magnifications.

### 3. Results

The mineralogical identification of the carbonaceous shale samples obtained from different depths of two boreholes analyzed using X-ray diffraction (XRD) values and patterns is presented in Table 1 and Figure 3a,b. The results show the presence of clay minerals composed of montmorillonite, mixed illite/smectite (I/S), illite, chlorite, and non-clay minerals such as dolomite, albite, microcline, pyrite, and quartz. The average quartz content was 29.42%, ranging from 25.10% to 35.60%. However, quartz with higher values was found at a depth of 470 m. The relatively high quartz content may be attributed to the preserved detrital silica input from associated siltstone facies, since it has high resistance to mechanical alteration, although diagenetic quartz can precipitate from the dissolution of feldspar [38,44].

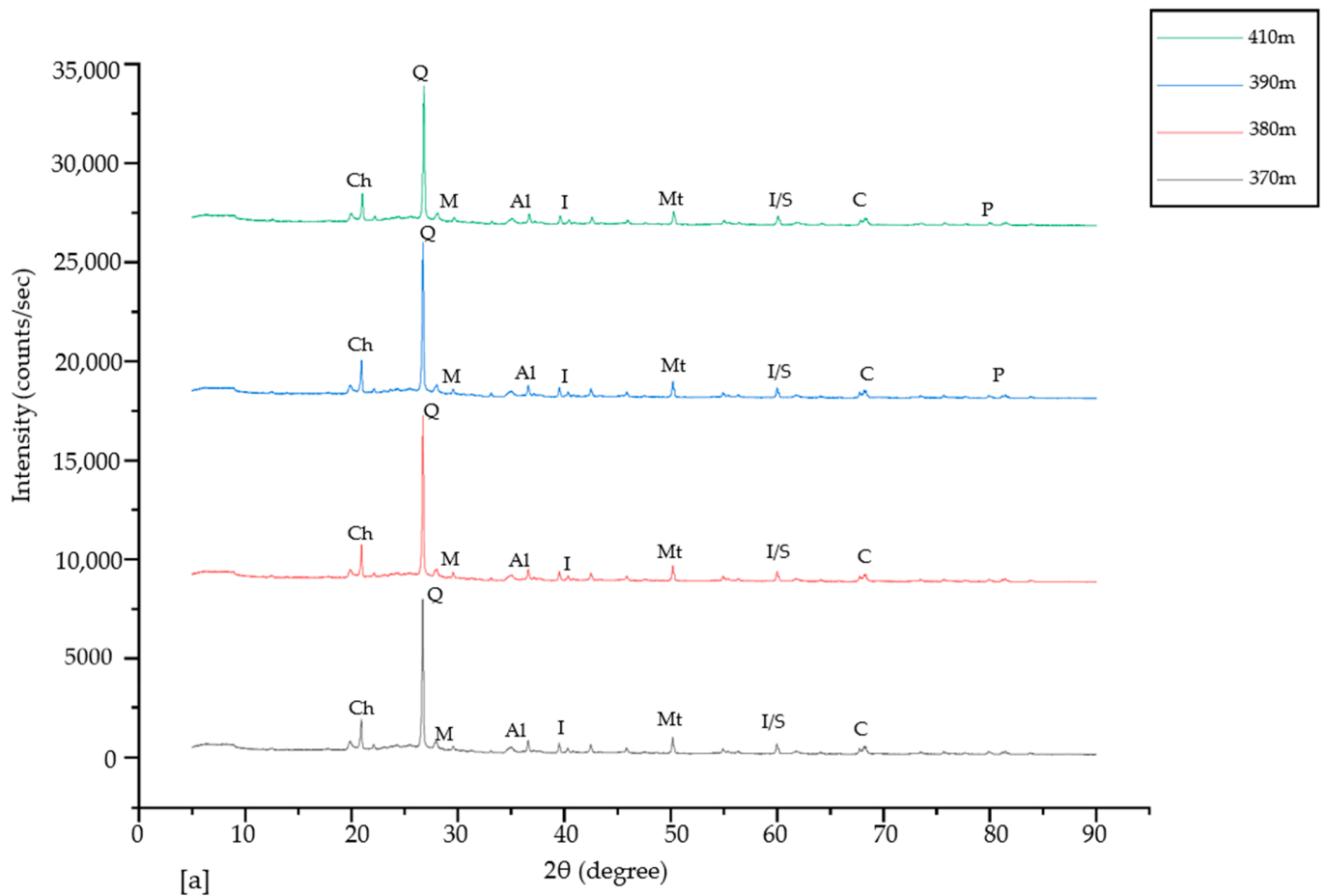
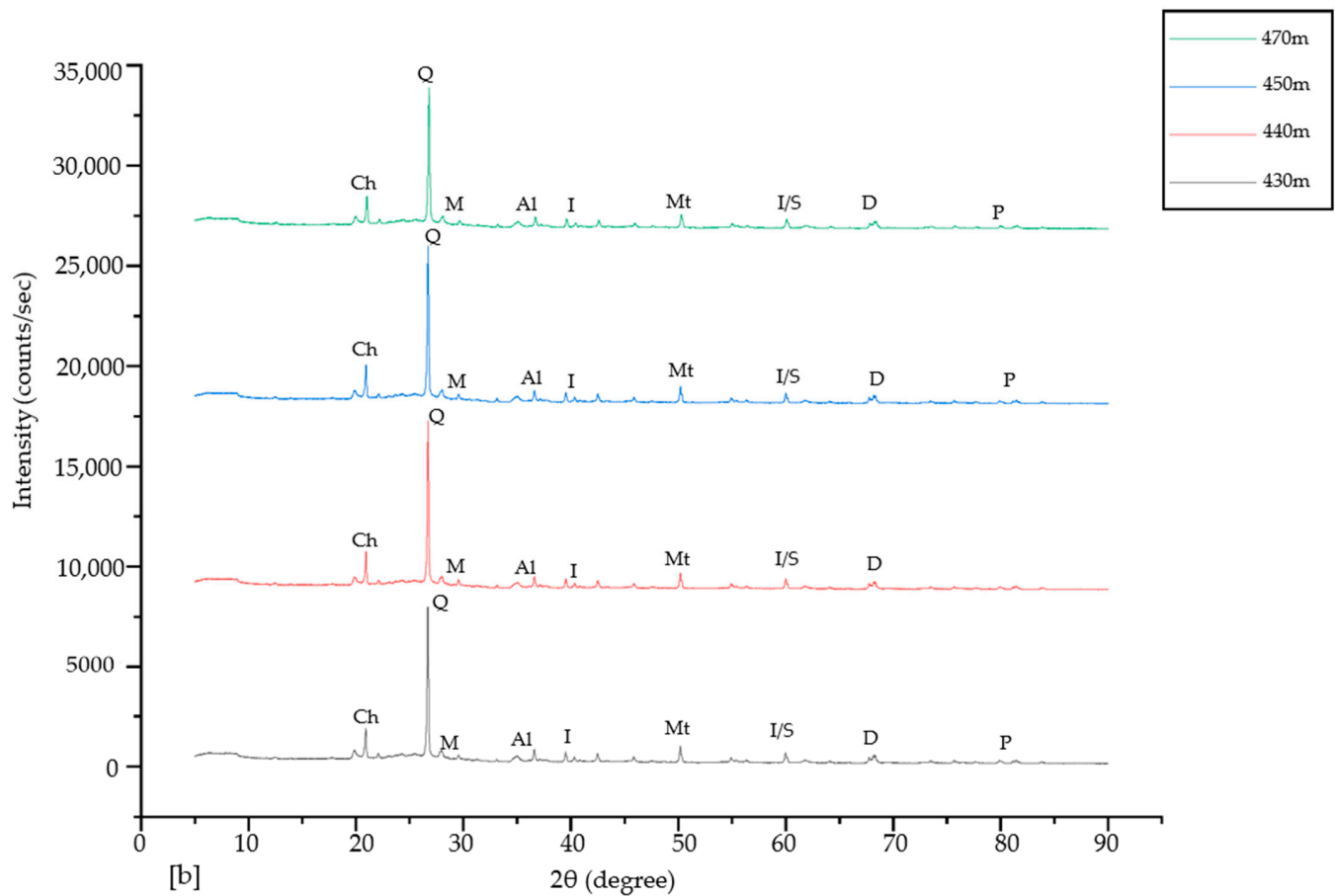


Figure 3. Cont.



**Figure 3.** X-ray diffractogram patterns of the studied carbonaceous shale from depth (a) 370 m to 410 m (b) 430 m to 470 m (note: ch-chlorite, Q—Quartz, M—Microcline, Al—Albite, I—Illite, Mt—Montmorillonite, I/S—mixed layer Illite-Smectite, C—Calcite, D—Dolomite, P—Pyrite).

**Table 1.** Mineral composition of the carbonaceous shale samples from different depths.

Sample ID	Formation	Depth (m)	Mineral Composition (%)									
			Qtz	Micr	Alb	Chl	Ill	I/S	Mont	Dol	Cal	Pyr
SBH1	Mikambeni	370	25.95	13.05	8.40	2.15	15.20	8.25	21.35	-	5.30	-
SBH2		380	25.10	12.85	7.25	2.70	16.80	9.80	21.90	-	4.40	-
SBH3		390	29.55	8.80	6.05	3.45	14.85	9.70	20.50	-	6.45	1.50
SBH4		410	25.75	10.45	4.90	3.55	15.90	9.05	18.05	-	8.80	3.02
SBH5		430	25.60	9.15	5.05	2.05	18.50	10.40	18.25	10.35	-	1.20
SBH6		440	33.02	9.50	4.45	3.73	19.26	11.98	9.85	7.30	-	1.00
SBH7		450	34.80	8.80	3.05	3.15	19.70	12.20	7.80	11.05	-	-
SBH8		470	35.60	9.75	-	4.05	20.50	13.20	5.40	10.65	-	1.50

Note: Qtz—Quartz, Micr—Microcline, Alb—Albite, Chl—Chlorite, Ill—Illite, I/S—Mixed Illite/Smectite, Mont—Montmorillonite, Dol—Dolomite, Calcite—Cal, Pyr—Pyrite.

In contrast to the quartz content, the average amount of microcline and albite was 10.17% and 5.45%. However, there is no albite mineral present at a depth of 470 m. Feldspars are susceptible to dissolution reaction as burial depth increases, as the albite minerals progressively reduce until the 470 m [45,46]. As burial depth increases, the montmorillonite content progressively decreases from 21.35% to 5.40%, while, on the other hand, the illite and mixed I/S contents increased from 15.20% to 20.50% and 8.25 to 13.20%. This observation is ascribed to the illitization reaction at burial depth temperature less than 200 °C in which precursor minerals of K-feldspar or smectite transform to illite or

mixed Smectite/illite (S/I) in the presence of sufficient  $K^+$  [47–49]. The chlorite content has an average value of 3.42% and ranges from 2.20% to 5.65% in a dispersed sequence in all samples. The presence of chlorite mineral suggests a by-product of the montmorillonite-illitization-chloritization transformation. This transformation process occurs in a closed system having a low ratio of fluid to shale rock [50]. The distribution of dolomite showed a progressive increment in concentration from 5.30 to 11.05 with burial depth. Since the organic-rich shale has a low fluid-to-rock ratio, the idea of dolomite replacing calcite with the saturated fluid of  $Mg^{2+}$  may not be feasible. The explanation is the precipitation of primary dolomite and stepwise recrystallization due to bacterial mediation [51]. It is worth noting that a high fluid–rock ratio is necessary for a steady and saturated supply of  $Mg^{2+}$  for dolomitization replacement of calcite, which favors permeable sandstone over impermeable buried shales. High burial temperature is insufficient to destroy the evidence of pyrite grain history or origin. Hence, its presence suggested detrital grain devoid of oxidizing setting but associated with anoxic, aridity, or fluvial settings [52,53].

The Fourier Transform Infrared (FTIR) spectra of the studied carbonaceous shale depict different absorbance bands of organic and mineral content at the various diagnostic wavelength of the infrared spectrum (Figure 4). Each absorbance band indicates the functional group representing the whole molecular structure of a material [30]. Most of the studied samples exhibit a strong characteristic absorbance peak around  $650\text{--}900\text{ cm}^{-1}$ , corresponding to the aromatic phenolic group,  $C=C\text{-OH}$ . However, the peak reduces as temperature increases with depth due to bond deformation [54]. The aromatic  $C=C$  absorption group suggests a wavelength band that is typical of terrigenous plants that have lignin-derivative materials [55]. The peak stretching from around  $1000\text{ cm}^{-1}$  to  $1220\text{ cm}^{-1}$  indicates the  $C\text{-O}$  stretching and  $OH$  deformation of the carboxylic,  $COOH$  groups, suggesting decarboxylation of organic matter [56]. The deformation of the carboxylic group releases the  $CO_2$ , reflecting a characteristic strong absorption around  $2000\text{--}2300\text{ cm}^{-1}$  [30]. However, the aliphatic hydrocarbon is considered to contain more carboxylic- and phenolic- $OH$  functional groups with a micelle-like structure that has a relative macromolecular weight ranging from 3500 to 100,000 Da compared with aromatic hydrocarbon [57]. In aromatic hydrocarbon, the voids among the carbon chain serve to act as trapping and binding sites for organic lipids and inorganic materials such as hydrous oxides and clay minerals [57]. The hydrocarbon gas,  $CH_4$ , shows infrared absorbance peaks between  $2850$  and  $3000\text{ cm}^{-1}$  due to aliphatic  $C\text{-H}$  stretching of methyl and methylene vibration [54,58]. The low absorption peak around  $3500\text{ cm}^{-1}$  corresponds to water desorption wavelength [59]. The spectra showed inconspicuous peaks of the carboxylic group at greater burial depths around 450 m, suggesting over-maturation of organic matter beyond the methanogenesis window.

Representative SEM images of the studied carbonaceous shales are presented in Figure 5a–d. The image depicts a mixture of pore structures, organic matter, and mineral contents. The image (Figure 5a) revealed conspicuous intragranular pores among grains of quartz, feldspars, chlorite, illite, carbonate, and pyrite minerals as shown by the XRD, forming an interconnected pore. The interconnected pores provide migration pathways for gaseous hydrocarbon during organic matter (OM) maturation [60]. The carbonate compound of calcite and dolomite was found to dominate the shale, with carbon elemental content ranging from 65% to 73% (Figure 6c). Furthermore, the organic matters were also hosted in the intragranular pores of mineral grain, which suggests dissolution cavity of carbonate minerals since intrapore of clay minerals such as feldspar is difficult to observe [61]. Non-spherical, closely packed polyframboidal pyrite was observed, which is affirmed by the multiple occurrences of Fe-elemental contents on the EDX result. The presence of the polyframboidal pyrites suggests an anaerobic condition that favors organic matter degradation and thermal maturation as burial depth increases [62]. The thermal maturity of the organic matter is further supported by the presence of fibrous chlorite and illite minerals (Figure 6d), which are index minerals for high-diagenetic temperature zone and quality hydrocarbon reservoirs [63].

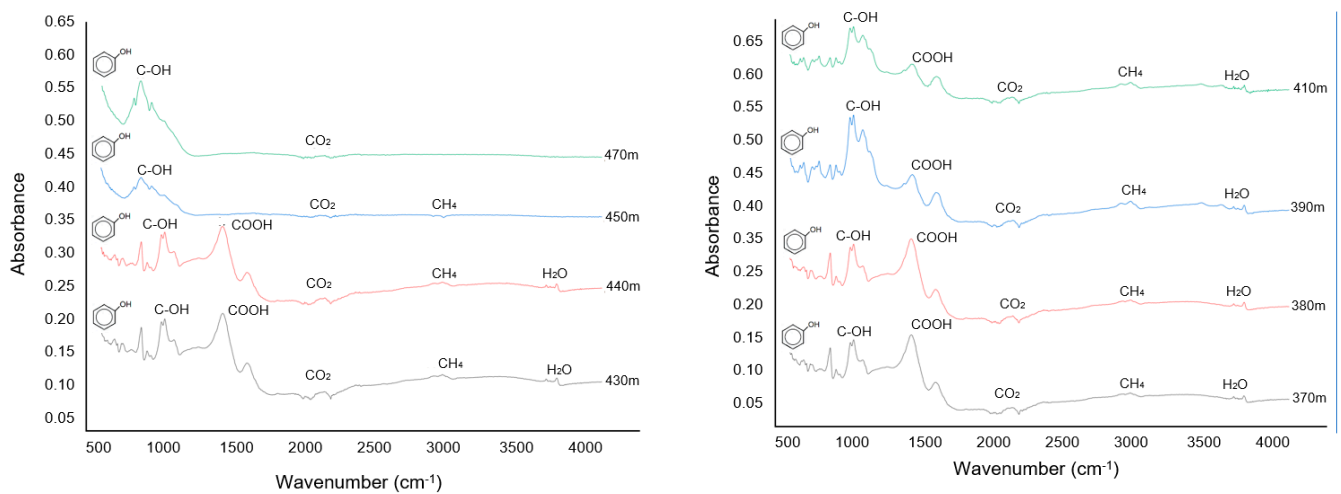


**Figure 4.** FTIR spectra of the studied carbonaceous shale showing functional groups representing molecules (R-OH-phenolic, C-C-OH-acetic, carboxylic, carbon (IV), COOH-carboxylic, CO<sub>2</sub>-carbon (IV) oxide, CH<sub>4</sub>-methane, H<sub>2</sub>O-water).

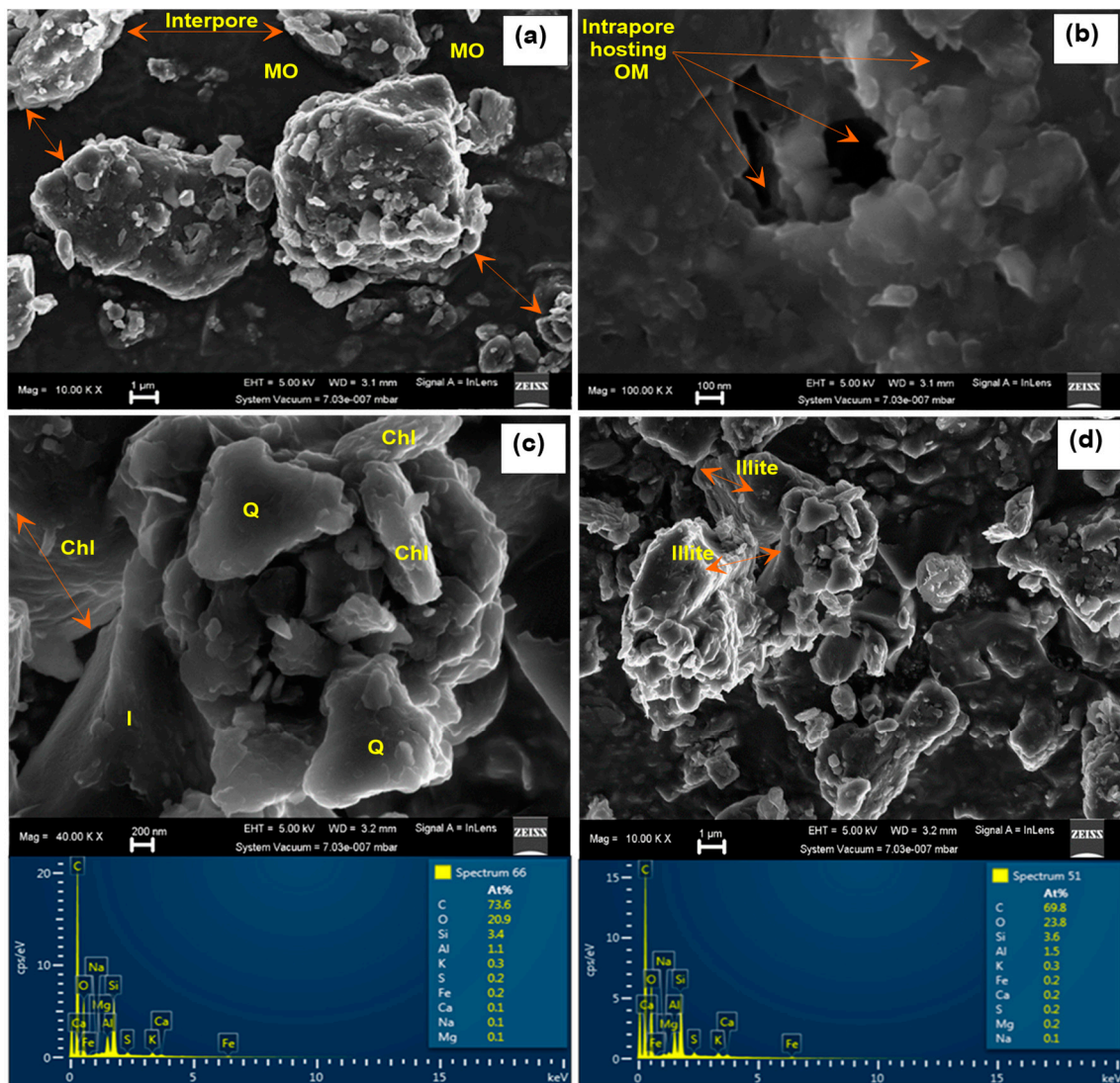


**Figure 5.** SEM images of the studied carbonaceous shale showing (a) intergranular pores hosting OM, (b) intragranular pores hosting OM, (c) SEM images of Chlorite-chl, Quartz-Q, Illite-I minerals, and (d) veinlet of Illite minerals.

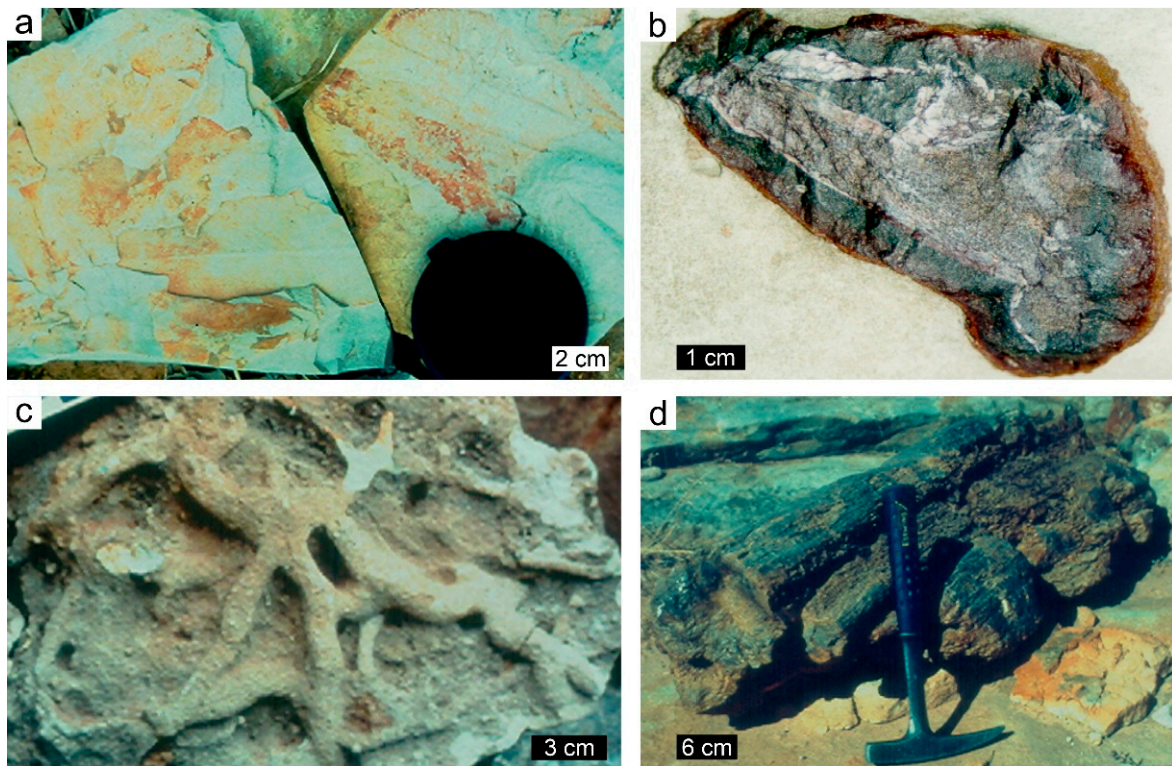


**Figure 6.** (a) vertical, cylindrical pipes with open apices, (b) simple, mostly vertical shaft-like trace fossils, (c) close up of the wall of the digit-like structure showing the extensively branching burrow system with random orientation (d) Large-scale trace fossils showing lateral bifurcations on a sub-horizontal surface (modified from [37]).

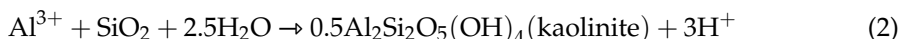
## 4. Discussion

### 4.1. Diagenetic Alteration Pathways

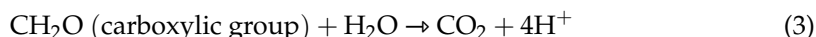
The mechanical compaction of detrital sediments and terrestrial plant materials following sedimentation of the 40 m thick Fripp Formation over Mikambeni Formation initiate their diagenetic changes. At this initial stage, the brackish interstitial fluid or pore water and bacterial activities are pronounced due to the degradation of plant material to produce humic material. Humic substances are composed of weak acidic electrolytes with aliphatic and aromatic hydrocarbon, which may incorporate atomic radicals N, O, or S [57]. The humic acid gains significance at a wavenumber absorption peak around  $650\text{--}900\text{ cm}^{-1}$ , corresponding to the acetic and phenolic group. The compaction process leads to dehydroxylation in which the pore fluid is released, as indicated by the water absorbance band around  $1300\text{--}1900\text{ cm}^{-1}$ . More evidence of the early-stage organic degradation in the Tuli Basin was marked the by bioturbation of burrowing organisms (Figure 6). In the studied basin, soft sediment burrowing organisms such as beetles and ants have produced un-bifurcated ichnofossils which are tentatively recognized as *Skolithosi* sp. and other bifurcated trace fossils [36].

With an increase in burial pressure and depth of about 360 m thick, which results from successive overlying sediments of the Solitude, Klopperfontein, Bosbokpoort, and Clarens formations, the elevated temperature causes further geochemical and mineralogical changes. The gradual decrease in montmorillonite and a parallel progressive increase of illite minerals were observed, while mixed-layered montmorillonite-illite (M-I) mark the extent of progress along with series of reactions between burial depths of about 370 m to 470 m. In Mikambeni shale, the first series of the illitization reaction progress is made possible due to the presence of microcline and montmorillonite minerals as expressed in Equation (1) [64]. Alternatively, diagenetic illite may have crystallized from geochemical interaction between kaolinite and microcline or potassium ion ( $\text{K}^+$ ), but the absence of

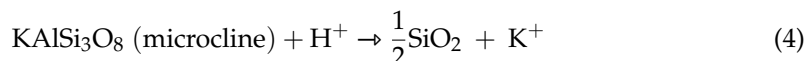
kaolinite inhibits that reaction's progress pathway. Retrospective studies [44,65] have reported the kaolinite illitization via reactions with k-feldspar,  $K^+$ , or  $H^+$  as burial depth increases; however, this reaction mechanism is hindered due to the absence of kaolinite minerals in Mikambeni shale. Kaolinites may have precipitated due to increasing quartz concentrations, but it is likely to be consumed immediately after crystallization as expressed in Equation (2) due to high temperature. Studies [66–68] have unequivocally demonstrated that the kaolinite dissolution in shale rock can take place at a lower temperature than 60 °C.



Furthermore, the organic and inorganic interaction promotes the illitization by initiating the release of the  $H^+$  ion from the carboxylic acid functional group as expressed in Equation (3). The carboxylic C=O band can remain approximately at a wavenumber of 1000 to 1225  $cm^{-1}$  stretching regardless of the source material. The  $CO_2$  produced by decarboxylation of organic matter is commonly suggested as a source of the acid that dissolves the microcline feldspar [69]. This carbon dioxide,  $CO_2$ , is recognized from its characteristic strong absorptions around 2000 and 2300  $cm^{-1}$ .



The presence of a carboxyl group increases solubility properties. As such, the labile microcline mineral interacts with the pore water concentrated with carboxylic and phenolic acids to produce silica and potassium cation, which enhances illitization of montmorillonite mineral as represented in Equation (4). This resulting authigenic silica likely contributes to the increasing quartz content with burial diagenesis, although the presence of preserved detrital quartz inputs cannot be discounted. With the siltstone facies interbedded with the carbonaceous shale, the input of detrital silica is possible since quartz is largely stable at high temperatures. Nonetheless, the increasing quartz contents tend to significantly improve the shale reservoir quality because it imparts a brittleness property and enhances the fracability of shale [70].

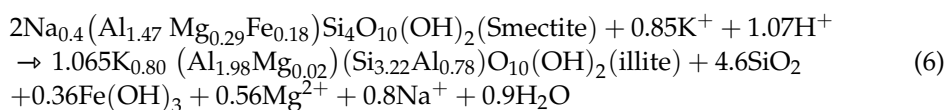


As the reaction continues, more  $K^+$  ions are concentrated via replacement K-feldspar (microcline) by the albite at a higher temperature between 120 °C and 180 °C as represented in Equation (5) [66,71]. The absence of kaolinite minerals with a parallel increase in chlorite suggests complete dissolution of kaolinite at such a high temperature.

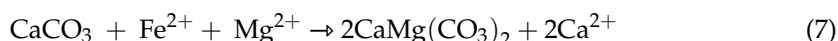


With further burial diagenesis, the presence of a high concentration of potassium  $K^+$  fluid promotes the illitization processes of montmorillonite minerals. However, other factors such as time, fluid/rock ratio, nature of starting material, and kinetic mechanism have been considered as important for illitization. It is worth noting that the direct conversion of smectite to illite as expressed in Equation (6) [72] does not suggest a solid-state reaction but rather shows the quantitative and compositional changes in shale mineralogy that takes place during burial diagenesis. Importantly, this conversion of smectite to illite reaction has been indicated to take place at similar temperature intervals as the maturation index for organic matter and the release of interstitial water during I-M diagenesis to enhance hydrocarbon migration [69]. By implication, the range for the change in I/S ordering from random to regular during smectite illitization in shales coincides with the

temperature range of organic matter maturity and the onset of oil generation in young sedimentary basins.



Although present in low quantities (Table 1), chlorite mineral is increasingly crystallized as a discrete phase rather than evolutionary trend phases of kaolinite and carbonate. The evolutionary phase involves the chloritization phase of kaolinite in the presence of iron- and magnesium-supplied smectite illitization processes at a temperature between 165 and 200 °C [73], but reaction progress is inhibited due to the absence of kaolinite. At a lower temperature of about 120 °C and in the presence of carbonate minerals, another chloritization reaction via kaolinite and iron oxide could occur [12,74]. The possible explanation for hydrothermal chloritization cannot be discounted in the Mikambeni carbonaceous shale owing to the presence of Sagole thermal spring via the Tshipise fault [75,76]. This interpretation is consistent with the chloritization processes reported at the geothermal area of Iceland in which iron-rich smectite (saponite) is transformed into mixed-layer smectite-chlorite (S-C) at about 200 to 230 °C [50]. In support of the S-C mixed layer, corrensite is a resulting mineral composed of 50% of each chlorite and smectite mineral [77]. With a further increase in temperature due to burial depth, chlorite crystallizes at temperatures greater than 240 °C due to a gradual replacement of iron-rich smectite with daughter chlorite mineral in close zonation contact [78]. This reaction mechanism suggests a solid-state gradual replacement; however, the reaction pathway may be a continuous series transition instead of a stepwise progression [79] since shale has a low pore fluid to rock ratio due to poor interconnectivity of pores. Stepwise transition is noted to predominate in the system with high pore-fluid-to-rock ratio such as sandstone; hence, chloritization in the studied shale may be a by-product of smectite illitization. Although the rise in temperature of diagenetic chlorite could be promoted by contact diagenesis associated with the Sagole geothermal area, the pore fluid of Mikambeni shale is unaffected by the thermal spring due to extremely highly impermeable shale. Carbonate minerals commonly revert to the thermodynamically stable mineral as dolomite replaces limestones in the deep-burial diagenetic realm, as represented in Equation (7) [79]. Calcite dissolution increases with burial dolomitization in the presence of an organic-rich and interstitial fluid via stepwise precipitation of dolomite.



The disappearance of calcite at relatively greater burial depths suggests a low pH medium, while its replacement by dolomite indicates an alkaline setting corresponding to oil window and organic matter maturation at a temperate range of 80–120 °C [80–82]. Promoted by sulfate reduction of pyrite mineral resulting from microbial activities, an increase in alkalinity medium favors precipitation of dolomite in the presence of Ca and Mg as burial depth increases [83]. The reduction process of  $\text{Fe}^{3+}$  to  $\text{Fe}^{2+}$  in the form of pyrite is evident from the framboidal structure revealed by SEM microscopy, thus suggesting a reducing or anoxic environment. Framboidal pyrites having bioclast structures that result from the reduction of organic matter in an organic-rich shale.

#### 4.2. Methanogenesis Potentials of the Carbonaceous Shale

The biogenic methanogenesis from diagenetic carbonaceous shale may be attributed both to microbial degradation of organic matters and their thermal maturation as burial depth increases (Figure 7). The carboxyl C=O stretching absorption peak, around 1000–1220  $\text{cm}^{-1}$ , is stronger in spectra. The presence carboxyl group increases solubility properties. The post-depositional activities of microbial degradation on organic matter of shale deposit tend

to produce biogenic methane, sulfide gases, and organic acids fluid capable of dissolving some reactive mineral phases.

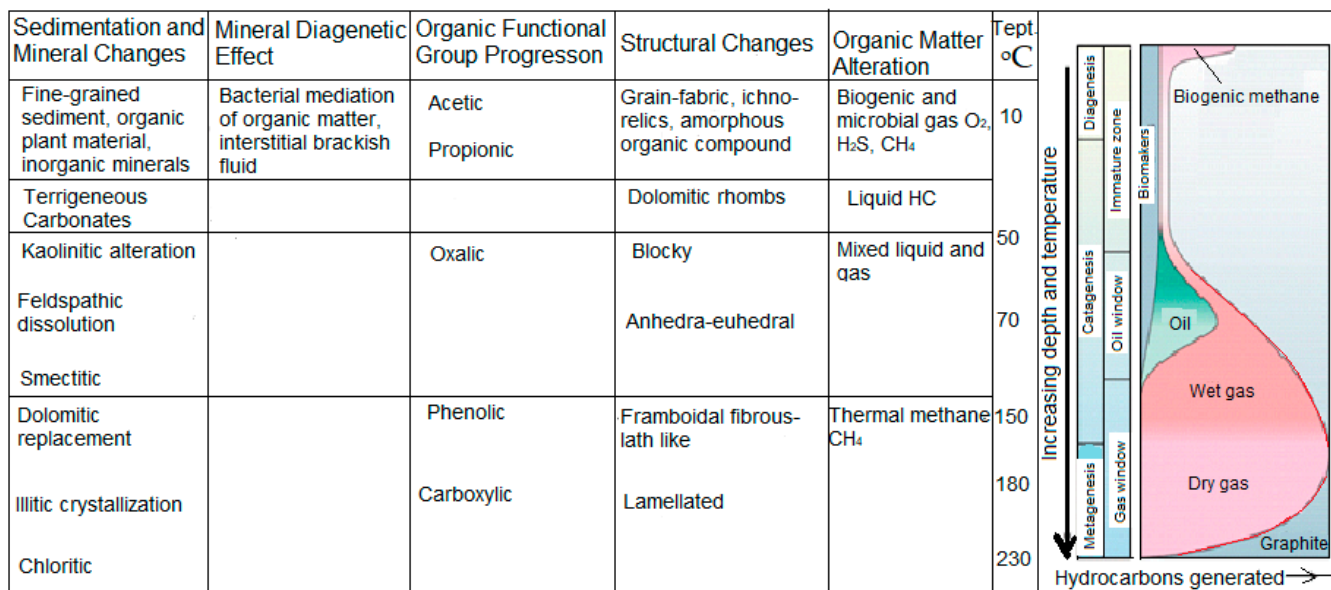


Figure 7. Methanogenesis potential of the studied carbonaceous shale.

Among the evidence of methanogenesis processes are the imprints of burrowing organisms, which suggest a connection with bioturbation processes capable of expelling biogenic gases from carbonaceous matter in shales [84]. The micro-FTIR revealed several linking bonds such as aromatic C=C stretching and amide group N=H bending in the acetic and propionic functional group, thus consistent with the organic macerals rich in protein, carbohydrate, lipids, and lignin [85]. At this stage, dewatering of pores first occurs at 10–50 °C, followed by biogenic methane from residual lignin at 50–70 °C (Figure 7) and characterized by carbonate minerals and acetic organic group. The water absorption spectra stretch between 3500 and 4000 cm<sup>-1</sup> wavenumber band. This observation alludes to the carbon δ<sup>13</sup>C isotopic analysis, which reported an acetoclastic decomposition of aliphatic to aromatic components with the generation of early methane gas [86].

At greater depth, the organic functional group comprising mainly phenolic and carboxylic, which were observed alongside mineralogical components of illite and chlorite was associated with thermal methanogenesis. At depths greater than 2500 m, recent studies [87] have established the presence of diagenetic illite and chlorite minerals to characterized geochemical zones in which the temperature is above 180 °C and the low metamorphic zone. Although the Mikambeni shale is shallower, the proximity of Sagole and Siloam geothermal fields may play a role in the elevated temperature that caused the diagenetic and thermal maturation of organic matter. The alteration in I-M ordering from random to regular during montmorillonite illitization and chloritization in shales coincides with the temperature range of organic matter maturity and the onset of the oil and gas window in the Mikambeni shale. Depending on the nature of the organic matter, marine diatoms and fora-minifera undergo a catagenesis at the oil window, while the terrestrial higher plant materials exceed catagenesis to methanogenesis at about 200 °C, as indicated by the organic carboxylic group [87,88]. The methane is indicated by a strong absorption band around 3015 cm<sup>-1</sup> and a band around 1305 cm<sup>-1</sup>.

The formation of solid carbon components involves a multi-stage process of kerogen degradation, initiated by deposition of organic matters [89]. Sources of organic matter could be either derived from the ocean, consisting of phytoplanktonic remains, or land, which consists mainly of vascular plant remains. However, accumulation of both marine and land-derived organic matter is common at deltas or floodplains of meandering rivers [90,91]. Under this oxic condition in the water column, the aerobic degradation of organic matter

continued until the dissolved oxygen was less than 0.2 mL/L H<sub>2</sub>O [92]. The deficiency in oxygen may be due to climatic overprint, sea-level changes, tectonic activities, and hydrographic factors, resulting in an insufficient supply of oxygen to oxidize the organic materials [93,94]. In addition, the faster rate of organic matter accumulation in sediments more than the aerobic degradation and bacterial oxidation processes may contribute to the enrichment of organic carbon beyond its decomposition [95]. Below 0.2 mL/L H<sub>2</sub>O oxygen concentration, anaerobic conditions and degradation of organic matter begin, giving rise to the solid carbon-containing components in shale sediments [95]. This anoxic setting is established as all the oxidants in the shale sediments deplete due to further reduction processes caused by increasing burial depth, promoting the activities of sulfide-reducing bacteria [96]. Studies [97–100] have highlighted minerals and compounds such as pyrite, sphalerite, hydrogen sulphide, and iron sulfide as evidence of the reduction process that ensued from sulfide-driven bacteria. With further increase in burial depth below the sediment–water interface, the methanogens begin to degrade the organic carbon to generate biogenic methane. This is consistent with the previous work of Tourtelot (1979), which argued that methane is unlikely to form unless all sulphates are depleted while vanadium and nickel are concentrated.

## 5. Conclusions

The combination of FTIR, SEM-EDX, and mineralogical analyses demonstrated a promising approach to assess methanogenesis potentials in carbonaceous shale rock. In shale rock that is dominated by terrigenous higher plants, the biogenic methanogenesis is found to correspond to the absorption spectrum stretching from 1650–1220 cm<sup>−1</sup> frequencies. This spectrum reflects the C-O stretching and OH deformation of acetic and phenolic groups in all studied samples. Given the strong absorptions around 2000–2300 cm<sup>−1</sup>, CO<sub>2</sub> is produced by decarboxylation of organic matter. The gas becomes acidified and dissolves feldspar to release K<sup>+</sup> ions, which promoted the illitization of smectite. The SEM microscopy depicted a framboidal structure, which indicated a sulfate reduction of pyrite mineral. The reduction process results from microbial activities in an anoxic milieu and causes an increase in alkalinity medium that favors precipitation of dolomite in the presence of Ca and Mg as burial depth increases. The contact diagenesis from the proximity of Sagole geothermal spring via Tshipise fault is suggested to have enhanced the transformation of smectite to chlorite via a mixed-layer corrensitite in a solid-state gradual replacement reaction pathway. The presence of diagenetic chlorite mineral is characteristic of low-grade metamorphism or high diagenetic zone at a temperature around 200–230 °C and corresponds to thermal breakdown of kerogen to methane at a strong absorption band around 2850–3000 cm<sup>−1</sup>.

**Author Contributions:** The conceptualization and writing of the original manuscript were conducted by G.O.A.; project administration and supervision by F.A.-D. and S.R.; formal analysis and methodology by N.P. and W.M.G.; resources, data curation, and software by S.E.M. and J.N.E. All authors have read and agreed to the published version of the manuscript.

**Funding:** This research received no external funding.

**Acknowledgments:** The authors are grateful for the assistance provided by Ally Mahlaule during the data collections.

**Conflicts of Interest:** The authors declare no conflict of interest.

## References

1. Dimitrov, R.S. The Paris agreement on climate change: Behind closed doors. *Glob. Environ. Politics* **2016**, *16*, 1–11. [[CrossRef](#)]
2. Vicedo-Cabrera, A.M.; Guo, Y.; Sera, F.; Huber, V.; Schleussner, C.-F.; Mitchell, D.; Tong, S.; Coelho, M.d.S.Z.S.; Saldiva, P.H.N.; Lavigne, E. Temperature-related mortality impacts under and beyond Paris Agreement climate change scenarios. *Clim. Chang.* **2018**, *150*, 391–402. [[CrossRef](#)]
3. Wollenberg, E.; Richards, M.; Smith, P.; Havlík, P.; Obersteiner, M.; Tubiello, F.N.; Herold, M.; Gerber, P.; Carter, S.; Reisinger, A. Reducing emissions from agriculture to meet the 2 C target. *Glob. Chang. Biol.* **2016**, *22*, 3859–3864. [[CrossRef](#)]

4. Wang, K.-H.; Su, C.-W.; Lobont, O.-R.; Umar, M. Whether crude oil dependence and CO<sub>2</sub> emissions influence military expenditure in net oil importing countries? *Energy Policy* **2021**, *153*, 112281. [[CrossRef](#)]
5. Guliyev, F. Trump's "America first" energy policy, contingency and the reconfiguration of the global energy order. *Energy Policy* **2020**, *140*, 111435. [[CrossRef](#)]
6. Mohtar, R.H.; Shafieezadeh, H.; Blake, J.; Daher, B. Economic, social, and environmental evaluation of energy development in the Eagle Ford shale play. *Sci. Total Environ.* **2019**, *646*, 1601–1614. [[CrossRef](#)]
7. Mohtar, R.H.; Daher, B. Lessons learned: Creating an interdisciplinary team and using a nexus approach to address a resource hotspot. *Sci. Total Environ.* **2019**, *650*, 105–110. [[CrossRef](#)]
8. Geel, C.; Schulz, H.-M.; Booth, P.; deWit, M.; Horsfield, B. Shale gas characteristics of Permian black shales in South Africa: Results from recent drilling in the Ecca Group (Eastern Cape). *Energy Procedia* **2013**, *40*, 256–265. [[CrossRef](#)]
9. Wang, J.; Liu, M.; Bentley, Y.; Feng, L.; Zhang, C. Water use for shale gas extraction in the Sichuan Basin, China. *J. Environ. Manag.* **2018**, *226*, 13–21. [[CrossRef](#)] [[PubMed](#)]
10. Thomas, M.; Partridge, T.; Harthorn, B.H.; Pidgeon, N. Deliberating the perceived risks, benefits, and societal implications of shale gas and oil extraction by hydraulic fracturing in the US and UK. *Nat. Energy* **2017**, *2*, 1–7. [[CrossRef](#)]
11. Mosavel, H.; Cole, D.; Siad, A. Shale gas potential of the Prince Albert Formation: A preliminary study. *S. Afr. J. Geol.* **2019**, *122*, 541–554. [[CrossRef](#)]
12. Dowe, P.J.; Taylor, K.G. Diagenetic mineral development within the Upper Jurassic Haynesville-Bossier Shale, USA. *Sedimentology* **2020**, *67*, 47–77. [[CrossRef](#)]
13. Baiyegunhi, C.; Liu, K.; Wagner, N.; Gwavava, O.; Oloninyi, T. Geochemical Evaluation of the Permian Ecca Shale in Eastern Cape Province, South Africa: Implications for Shale Gas Potential. *Acta Geol. Sin. Engl. Ed.* **2018**, *92*, 1193–1217. [[CrossRef](#)]
14. Liu, Y.; Hou, J. Investigation on the potential relationships between geophysical properties and CH<sub>4</sub> adsorption in a typical shale gas reservoir. *Energy Fuels* **2019**, *33*, 8354–8362. [[CrossRef](#)]
15. Zhu, Y.; Liu, E.; Martinez, A.; Payne, M.A.; Harris, C.E. Understanding geophysical responses of shale-gas plays. *Lead. Edge* **2011**, *30*, 332–338. [[CrossRef](#)]
16. Schovsbo, N.H.; Nielsen, A.T.; Klitten, K.; Mathiesen, A.; Rasmussen, P. Shale gas investigations in Denmark: Lower Palaeozoic shales on Bornholm. *Geol. Surv. Den. Greenl. (GEUS) Bull.* **2011**, *23*, 9–12. [[CrossRef](#)]
17. Ola, P.S.; Aidi, A.K.; Bankole, O.M. Clay mineral diagenesis and source rock assessment in the Bornu Basin, Nigeria: Implications for thermal maturity and source rock potential. *Mar. Pet. Geol.* **2018**, *89*, 653–664. [[CrossRef](#)]
18. Zheng, Y.; Liao, Y.; Wang, Y.; Xiong, Y. Organic geochemical characteristics, mineralogy, petrophysical properties, and shale gas prospects of the Wufeng-Longmaxi shales in Sanquan Town of the Nanchuan District, Chongqing. *AAPG Bull.* **2018**, *102*, 2239–2265. [[CrossRef](#)]
19. Washburn, K.E. Rapid geochemical and mineralogical characterization of shale by laser-induced breakdown spectroscopy. *Org. Geochem.* **2015**, *83*, 114–117. [[CrossRef](#)]
20. Bernard, S.; Horsfield, B.; Schulz, H.-M.; Wirth, R.; Schreiber, A.; Sherwood, N. Geochemical evolution of organic-rich shales with increasing maturity: A STXM and TEM study of the Posidonia Shale (Lower Toarcian, northern Germany). *Mar. Pet. Geol.* **2012**, *31*, 70–89. [[CrossRef](#)]
21. Zuo, X.; Li, C.; Zhang, J.; Ma, G.; Chen, P. Geochemical characteristics and depositional environment of the Shahejie Formation in the Binnan Oilfield, China. *J. Geophys. Eng.* **2020**, *17*, 539–551. [[CrossRef](#)]
22. Ibad, S.M.; Padmanabhan, E. Methane sorption capacities and geochemical characterization of Paleozoic shale Formations from Western Peninsula Malaysia: Implication of shale gas potential. *Int. J. Coal Geol.* **2020**, *224*, 103480. [[CrossRef](#)]
23. Owusu, E.B.; Tsegab, H.; Sum, C.W.; Padmanabhan, E. Organic geochemical analyses of the Belata black shale, Peninsular Malaysia; implications on their shale gas potential. *J. Nat. Gas Sci. Eng.* **2019**, *69*, 102945. [[CrossRef](#)]
24. Xi, Z.; Tang, S.; Wang, J. The reservoir characterization and shale gas potential of the Niutitang formation: Case study of the SY well in northwest Hunan Province, South China. *J. Pet. Sci. Eng.* **2018**, *171*, 687–703. [[CrossRef](#)]
25. Liang, C.; Jiang, Z.; Cao, Y.; Zhang, J.; Guo, L. Sedimentary characteristics and paleoenvironment of shale in the Wufeng-Longmaxi Formation, North Guizhou Province, and its shale gas potential. *J. Earth Sci.* **2017**, *28*, 1020–1031. [[CrossRef](#)]
26. Tuo, J.; Wu, C.; Zhang, M. Organic matter properties and shale gas potential of Paleozoic shales in Sichuan Basin, China. *J. Nat. Gas Sci. Eng.* **2016**, *28*, 434–446. [[CrossRef](#)]
27. Wang, R.; Sang, S.; Jin, J.; Zhao, L.; Gao, W.; Fu, W.; Shi, F.; Deng, E. Characteristics and significance of heterogeneity of sea-land transitional facies shale gas reservoir in North Guizhou, China. *Geosci. J.* **2019**, *23*, 101–117. [[CrossRef](#)]
28. Anovitz, L.M.; Cole, D.R. Analysis of the Pore Structures of Shale Using Neutron and X-ray Small Angle Scattering. In *Geological Carbon Storage: Subsurface Seals and Caprock Integrity*; Wiley: Hoboken, NJ, USA, 2018; pp. 71–118.
29. Lee, K.S.; Kim, T.H. *Transport in Shale Reservoirs*; Gulf Professional Publishing: Houston, TX, USA, 2019.
30. Washburn, K.E.; Birdwell, J.E. Multivariate analysis of ATR-FTIR spectra for assessment of oil shale organic geochemical properties. *Org. Geochem.* **2013**, *63*, 1–7. [[CrossRef](#)]
31. Bordy, E. Lithostratigraphy of the Tshidzi Formation (Dwyka Group, Karoo Supergroup), South Africa. *S. Afr. J. Geol.* **2018**, *121*, 109–118. [[CrossRef](#)]
32. Bordy, E.M. *Sedimentology of the Karoo Supergroup in the Tuli Basin*; Rhodes University: Grahamstown, South Africa, 2000.
33. Jeffrey, L. Characterization of the coal resources of South Africa. *J. S. Afr. Inst. Min. Metall.* **2005**, *105*, 95–102.

34. Denge, E.; Baiyegunhi, C. Maceral Types and Quality of Coal in the Tuli Coalfield: A Case Study of Coal in the Madzaringwe Formation in the Vele Colliery, Limpopo Province, South Africa. *Appl. Sci.* **2021**, *11*, 2179. [[CrossRef](#)]
35. Catuneanu, O.; Hancox, P.; Rubidge, B. Reciprocal flexural behaviour and contrasting stratigraphies: A new basin development model for the Karoo retroarc foreland system, South Africa. *Basin Res.* **1998**, *10*, 417–439. [[CrossRef](#)]
36. Bordy, E.M.; Catuneanu, O. Sedimentology and palaeontology of upper Karoo aeolian strata (Early Jurassic) in the Tuli Basin, South Africa. *J. Afr. Earth Sci.* **2002**, *35*, 301–314. [[CrossRef](#)]
37. Bordy, E.M.; Catuneanu, O. Sedimentology of the Beaufort-Molteno Karoo fluvial strata in the Tuli Basin, South Africa. *S. Afr. J. Geol.* **2002**, *105*, 51–66. [[CrossRef](#)]
38. Johnson, M.; Anhaeuser, C.; Thomas, R.J. The Geology of South Africa: Geological Society of South Africa. *Counc. Geosci. Pretoria.* **2006**, *691*, 461–500.
39. Chidley, C. The geology of the country around Evangelina and Pontdrift (1:50,000 sheets 2228BD and 2229A). In *Unpublished South African Geological Survey Report*; Council of Geosciences South Africa Report: Pietersburg, South Africa, 1985; p. 22. A.
40. Jung, J.; Yoo, K.-C.; Lee, K.-H.; Park, Y.K.; Lee, J.I.; Kim, J. Clay Mineralogical Characteristics of Sediments Deposited during the Late Quaternary in the Larsen Ice Shelf B Embayment, Antarctica. *Minerals* **2019**, *9*, 153. [[CrossRef](#)]
41. Hasan, M.N.; Yeasmin, R.; Rahman, M.; Potter-McIntyre, S. Diagenetic Clay Minerals and Their Controls on Reservoir Properties of the Shahbazpur Gas Field (Bengal Basin, Bangladesh). *Geosciences* **2020**, *10*, 250. [[CrossRef](#)]
42. Akintola, G.O.; Amponsah-Dacosta, F.; Mhlongo, S.E. Geotechnical evaluation of clayey materials for quality burnt bricks. *Heliyon* **2020**, *6*, e05626. [[CrossRef](#)] [[PubMed](#)]
43. Jaboyedoff, M.; Bussy, F.; Kübler, B.; Thelin, P. Illite “crystallinity” revisited. *Clays Clay Miner.* **2001**, *49*, 156–167. [[CrossRef](#)]
44. Baiyegunhi, C.; Liu, K.; Gwavava, O. Diagenesis and reservoir properties of the permian Ecca Group sandstones and mudrocks in the Eastern Cape Province, South Africa. *Minerals* **2017**, *7*, 88. [[CrossRef](#)]
45. Yuan, G.; Cao, Y.; Zan, N.; Schulz, H.-M.; Gluyas, J.; Hao, F.; Jin, Q.; Liu, K.; Wang, Y.; Chen, Z.; et al. Coupled mineral alteration and oil degradation in thermal oil-water-feldspar systems and implications for organic-inorganic interactions in hydrocarbon reservoirs. *Geochim. Cosmochim. Acta* **2019**, *248*, 61–87. [[CrossRef](#)]
46. Yuan, G.; Cao, Y.; Gluyas, J.; Jia, Z. Reactive transport modeling of coupled feldspar dissolution and secondary mineral precipitation and its implication for diagenetic interaction in sandstones. *Geochim. Cosmochim. Acta* **2017**, *207*, 232–255. [[CrossRef](#)]
47. Liang, C.; Cao, Y.; Liu, K.; Jiang, Z.; Wu, J.; Hao, F. Diagenetic variation at the lamina scale in lacustrine organic-rich shales: Implications for hydrocarbon migration and accumulation. *Geochim. Cosmochim. Acta* **2018**, *229*, 112–128. [[CrossRef](#)]
48. Berger, G.; Lacharpagne, J.-C.; Velde, B.; Beaufort, D.; Lanson, B. Kinetic constraints on illitization reactions and the effects of organic diagenesis in sandstone/shale sequences. *Appl. Geochem.* **1997**, *12*, 23–35. [[CrossRef](#)]
49. Kennedy, M.J.; Löhr, S.C.; Fraser, S.A.; Baruch, E.T. Direct evidence for organic carbon preservation as clay-organic nanocomposites in a Devonian black shale; from deposition to diagenesis. *Earth Planet. Sci. Lett.* **2014**, *388*, 59–70. [[CrossRef](#)]
50. Beaufort, D.; Rigault, C.; Billon, S.; Billault, V.; Inoue, A.; Inoué, S.; Patrier, P.; Ferrage, E. Chlorite and chloritization processes through mixed-layer mineral series in low-temperature geological systems—A review. *Clay Miner.* **2015**, *50*, 497–523. [[CrossRef](#)]
51. Montanez, I.P.; Read, J.F. Fluid-rock interaction history during stabilization of early dolomites, upper Knox Group (Lower Ordovician), US Appalachians. *J. Sediment. Res.* **1992**, *62*, 753–778.
52. Johnson, J.E.; Gerpheide, A.; Lamb, M.P.; Fischer, W.W. O<sub>2</sub> constraints from Paleoproterozoic detrital pyrite and uraninite. *Bulletin* **2014**, *126*, 813–830.
53. da Costa, G.; Hofmann, A.; Agangi, A. A revised classification scheme of pyrite in the Witwatersrand Basin and application to placer gold deposits. *Earth-Sci. Rev.* **2020**, *201*, 103064. [[CrossRef](#)]
54. Günzler, H.; Gremlich, H.-U. *IR Spectroscopy: An Introduction*; Wiley: Hoboken, NJ, USA, 2002.
55. Naseem, A.; Tabasum, S.; Zia, K.M.; Zuber, M.; Ali, M.; Noreen, A. Lignin-derivatives based polymers, blends and composites: A review. *Int. J. Biol. Macromol.* **2016**, *93*, 296–313. [[CrossRef](#)] [[PubMed](#)]
56. Dutta, S.; Hartkopf-Fröder, C.; Witte, K.; Brocke, R.; Mann, U. Molecular characterization of fossil palynomorphs by transmission micro-FTIR spectroscopy: Implications for hydrocarbon source evaluation. *Int. J. Coal Geol.* **2013**, *115*, 13–23. [[CrossRef](#)]
57. Hillel, D.; Hatfield, J.L. *Encyclopedia of Soils in the Environment*; Elsevier: Amsterdam, The Netherlands, 2005; Volume 3.
58. Baker, M.J.; Trevisan, J.; Bassan, P.; Bhargava, R.; Butler, H.J.; Dorling, K.M.; Fielden, P.R.; Fogarty, S.W.; Fullwood, N.J.; Heys, K.A. Using Fourier transform IR spectroscopy to analyze biological materials. *Nat. Protoc.* **2014**, *9*, 1771. [[CrossRef](#)]
59. Coenen, K.; Gallucci, F.; Mezari, B.; Hensen, E.; van Sint Annaland, M. An in-situ IR study on the adsorption of CO<sub>2</sub> and H<sub>2</sub>O on hydrotalcites. *J. CO<sub>2</sub> Util.* **2018**, *24*, 228–239. [[CrossRef](#)]
60. Xu, S.; Gou, Q.; Hao, F.; Zhang, B.; Shu, Z.; Lu, Y.; Wang, Y. Shale pore structure characteristics of the high and low productivity wells, Jiaoshiba Shale Gas Field, Sichuan Basin, China: Dominated by lithofacies or preservation condition? *Mar. Pet. Geol.* **2020**, *114*, 104211. [[CrossRef](#)]
61. Han, C.; Jiang, Z.; Han, M.; Wu, M.; Lin, W. The lithofacies and reservoir characteristics of the Upper Ordovician and Lower Silurian black shale in the Southern Sichuan Basin and its periphery, China. *Mar. Pet. Geol.* **2016**, *75*, 181–191. [[CrossRef](#)]
62. Cruz-Ceballos, L.F.; García-González, M.; Cruz-Guevara, L.E.; Avendaño-Sánchez, G.M. Geochemical Characterization and Thermal Maturation of Cerrejón Formation: Implications for the Petroleum System in the Ranchería Sub-Basin, Colombia. *Geosciences* **2020**, *10*, 258. [[CrossRef](#)]

63. Worden, R.; Utley, J.E.; Butcher, A.R.; Griffiths, J.; Wooldridge, L.; Lawan, A. Improved imaging and analysis of chlorite in reservoirs and modern day analogues: New insights for reservoir quality and provenance. *Geol. Soc. Lond. Spec. Publ.* **2020**, *484*, 189–204. [[CrossRef](#)]
64. Essene, E.; Peacor, D. Clay mineral thermometry—A critical perspective. *Clays Clay Miner.* **1995**, *43*, 540–553. [[CrossRef](#)]
65. Yuan, G.; Cao, Y.; Schulz, H.-M.; Hao, F.; Gluyas, J.; Liu, K.; Yang, T.; Wang, Y.; Xi, K.; Li, F. A review of feldspar alteration and its geological significance in sedimentary basins: From shallow aquifers to deep hydrocarbon reservoirs. *Earth-Sci. Rev.* **2019**, *191*, 114–140. [[CrossRef](#)]
66. Curtis, C.D. Clay mineral precipitation and transformation during burial diagenesis. *Philos. Trans. R. Soc. Lond. Ser. A Math. Phys. Sci.* **1985**, *315*, 91–105.
67. Thyberg, B.; Jahren, J. Quartz cementation in mudstones: Sheet-like quartz cement from clay mineral reactions during burial. *Pet. Geosci.* **2011**, *17*, 53–63. [[CrossRef](#)]
68. Metwally, Y.M.; Chesnokov, E.M. Clay mineral transformation as a major source for authigenic quartz in thermo-mature gas shale. *Appl. Clay Sci.* **2012**, *55*, 138–150. [[CrossRef](#)]
69. Lynch, F.L.; Mack, L.E.; Land, L.S. Burial diagenesis of illite/smectite in shales and the origins of authigenic quartz and secondary porosity in sandstones. *Geochim. Cosmochim. Acta* **1997**, *61*, 1995–2006. [[CrossRef](#)]
70. Ye, Y.; Tang, S.; Xi, Z. Brittleness Evaluation in Shale Gas Reservoirs and Its Influence on Fracability. *Energies* **2020**, *13*, 388. [[CrossRef](#)]
71. Bjørlykke, K.; Jahren, J. Open or closed geochemical systems during diagenesis in sedimentary basins: Constraints on mass transfer during diagenesis and the prediction of porosity in sandstone and carbonate reservoirs. *Geohorizon. AAPG Bull.* **2012**, *96*, 2193–2214. [[CrossRef](#)]
72. Huang, W.-L.; Longo, J.M.; Pevear, D.R. An experimentally derived kinetic model for smectite-to-illite conversion and its use as a geothermometer. *Clays Clay Miner.* **1993**, *41*, 162–177. [[CrossRef](#)]
73. Boles, J.R.; Franks, S.G. Clay diagenesis in Wilcox sandstones of Southwest Texas; implications of smectite diagenesis on sandstone cementation. *J. Sediment. Res.* **1979**, *49*, 55–70.
74. Muffler, L.J.; White, D.E. Active metamorphism of upper Cenozoic sediments in the Salton Sea geothermal field and the Salton Trough, southeastern California. *Geol. Soc. Am. Bull.* **1969**, *80*, 157–182. [[CrossRef](#)]
75. Johnson, M.R.; Van Vuuren, C.J.; Visser, J.N.; Cole, D.I.; Wickens, H.d.V.; Christie, A.D.; Roberts, D.L.; Brandl, G. Sedimentary rocks of the Karoo Supergroup. *Geol. S. Afr.* **2006**, 461–499.
76. Olivier, J.; Venter, J.; Jonker, C. Thermal and chemical characteristics of hot water springs in the northern part of the Limpopo Province, South Africa. *Water Sa* **2011**, *37*, 427–436. [[CrossRef](#)]
77. Huggett, J. *Clay Minerals, Reference Module in Earth Systems and Environmental Sciences*; Elsevier: Amsterdam, The Netherlands, 2015.
78. Yeblen, D.R. Electron microscopy applied to nonstoichiometry, polysomatism, and replacement reactions in minerals. In *Minerals and Reactions at the Atomic Scale*; De Gruyter: Berlin, Germany, 2018; pp. 181–230.
79. Swart, P.K. The geochemistry of carbonate diagenesis: The past, present and future. *Sedimentology* **2015**, *62*, 1233–1304. [[CrossRef](#)]
80. Montañez, I.P. Late diagenetic dolomitization of Lower Ordovician, upper Knox carbonates: A record of the hydrodynamic evolution of the southern Appalachian Basin. *AAPG Bull.* **1994**, *78*, 1210–1239.
81. Machel, H.G. Investigations of burial diagenesis in carbonate hydrocarbon reservoir rocks. *Geosci. Can.* **2005**, *32*, 103.
82. Montañez, I.; Crossey, L. Diagenesis. In *Encyclopedia of Geochemistry*; White, W.M., Ed.; Encyclopedia of Earth Sciences Series; Springer: Berlin/Heidelberg, Germany, 2017.
83. Morad, S. *Carbonate Cementation in Sandstones: Distribution Patterns and Geochemical Evolution*; John Wiley & Sons: Hoboken, NJ, USA, 2009; Volume 72.
84. Wang, Q.; Guo, H.; Wang, H.; Urynowicz, M.A.; Hu, A.; Yu, C.-P.; Fallgren, P.; Jin, S.; Zheng, H.; Zeng, R.J. Enhanced production of secondary biogenic coalbed natural gas from a subbituminous coal treated by hydrogen peroxide and its geochemical and microbiological analyses. *Fuel* **2019**, *236*, 1345–1355. [[CrossRef](#)]
85. Liu, B.; Schieber, J.; Mastalerz, M.; Teng, J. Organic matter content and type variation in the sequence stratigraphic context of the Upper Devonian New Albany Shale, Illinois Basin. *Sediment. Geol.* **2019**, *383*, 101–120. [[CrossRef](#)]
86. Flores, R.M.; Rice, C.A.; Stricker, G.D.; Warden, A.; Ellis, M.S. Methanogenic pathways of coal-bed gas in the Powder River Basin, United States: The geologic factor. *Int. J. Coal Geol.* **2008**, *76*, 52–75. [[CrossRef](#)]
87. McDonald, S.; Bishop, A.G.; Prenzler, P.D.; Robards, K. Analytical chemistry of freshwater humic substances. *Anal. Chim. Acta* **2004**, *527*, 105–124. [[CrossRef](#)]
88. Tetiker, S.; Yalçın, H.; Bozkaya, Ö. Approaches to the low grade metamorphic history of the Karakaya complex by chlorite mineralogy and geochemistry. *Minerals* **2015**, *5*, 221–246. [[CrossRef](#)]
89. Kotov, S.; Stolyarov, S.; Cazeneuve, E.; Wallis, F.; Gadzhimirzaev, D. Looking beyond the Wellbore: Formation Evaluation Mitigates Risk and Reduces Uncertainty in Multi-Stage Unconventional Completions. In Proceedings of the Abu Dhabi International Petroleum Exhibition & Conference, Abu Dhabi, United Arab Emirates, 13–16 November 2017; Society of Petroleum Engineers: Abu Dhabi, UAE.
90. Das, A.; Majumder, S.; Barman, S.; Chatterjee, D.; Mukhopadhyay, S.; Ghosh, P.; Pal, C.N.; Saha, G. Influence of basin-wide geomorphology on arsenic distribution in Nadia district. *Environ. Res.* **2021**, *192*, 110314. [[CrossRef](#)] [[PubMed](#)]

91. Lambert, T.; Teodoru, C.R.; Nyoni, F.C.; Bouillon, S.; Darchambeau, F.; Massicotte, P.; Borges, A.V. Along-stream transport and transformation of dissolved organic matter in a large tropical river. *Biogeosciences* **2016**, *13*, 2727–2741. [[CrossRef](#)]
92. Tyson, R. *Sedimentary Organic Matter: Organic Facies and Palynofacies*; Springer Science & Business Media: Berlin/Heidelberg, Germany, 2012.
93. Dean, W.E.; Arthur, M.A. Iron-sulfur-carbon relationships in organic-carbon-rich sequences I: Cretaceous Western Interior Seaway. *Am. J. Sci.* **1989**, *289*, 708–743. [[CrossRef](#)]
94. Dar, S.A.; Khan, K.; Birch, W. Sedimentary: Phosphates. In *Reference Module in Earth Systems and Environmental Sciences*; Elsevier: Amsterdam, The Netherlands, 2017; Volume 10.
95. Ferriday, T.; Montenari, M. Chemostratigraphy and Chemofacies of Source Rock Analogues: A High-Resolution Analysis of Black Shale Successions from the Lower Silurian Formigoso Formation (Cantabrian Mountains, NW Spain). In *Stratigraphy & Timescales*; Elsevier: Amsterdam, The Netherlands, 2016; Volume 1, pp. 123–255.
96. Capotondi, L.; Girone, A.; Lirer, F.; Bergami, C.; Verducci, M.; Vallefucio, M.; Afferri, A.; Ferraro, L.; Pelosi, N.; De Lange, G.J. Central Mediterranean Mid-Pleistocene paleoclimatic variability and its association with global climate. *Palaeogeogr. Palaeoclimatol. Palaeoecol.* **2016**, *442*, 72–83. [[CrossRef](#)]
97. Gallagher, S.J.; Kitamura, A.; Iryu, Y.; Itaki, T.; Koizumi, I.; Hoiles, P.W. The Pliocene to recent history of the Kuroshio and Tsushima Currents: A multi-proxy approach. *Prog. Earth Planet. Sci.* **2015**, *2*, 1–23. [[CrossRef](#)]
98. Sabino, M.; Schefuß, E.; Natalicchio, M.; Pierre, F.D.; Birgel, D.; Bortels, D.; Schnetger, B.; Peckmann, J. Climatic and hydrologic variability in the northern Mediterranean across the onset of the Messinian salinity crisis. *Palaeogeogr. Palaeoclimatol. Palaeoecol.* **2020**, *545*, 109632. [[CrossRef](#)]
99. Natalicchio, M.; Pierre, F.D.; Birgel, D.; Brumsack, H.; Carnevale, G.; Gennari, R.; Gier, S.; Lozar, F.; Pellegrino, L.; Sabino, M. Paleoenvironmental change in a precession-paced succession across the onset of the Messinian salinity crisis: Insight from element geochemistry and molecular fossils. *Palaeogeogr. Palaeoclimatol. Palaeoecol.* **2019**, *518*, 45–61. [[CrossRef](#)]
100. Reolid, M.; Duarte, L.; Rita, P. Changes in foraminiferal assemblages and environmental conditions during the T-OAE (Early Jurassic) in the northern Lusitanian Basin, Portugal. *Palaeogeogr. Palaeoclimatol. Palaeoecol.* **2019**, *520*, 30–43. [[CrossRef](#)]